Energy Advances

ROYAL SOCIETY OF CHEMISTRY

PAPER

View Article Online
View Journal | View Issue

Cite this: *Energy Adv.*, 2024, 3, 2613

Sustainable fermentable sugar production using a glass fiber supported gallium–molybdenum photocatalyst towards bioethanol production: LCA analysis†

Rajat Chakraborty, * Sourav Barman and Aritro Sarkar

For the first time, a cost-effective glass fiber (GF) support derived from waste printed circuit boards (W-PCBs) was utilized to synthesize a reusable GF-supported gallium–molybdenum photocatalyst (GaMo–GF) for generating fermentable sugar (FS) from delignified corncob (DCC) in a quartz halogen solar batch reactor (QHSR). Additionally, this paper presents a comparative detoxification investigation and subsequent fermentation of the resulting FS using *Pichia stipitis*. The optimum Ga^4Mo-GF (with a gallium precursor loading of 4 wt%) photocatalyst exhibited impressive characteristics, including a high specific surface area (28.01 $m^2\ g^{-1}$), high pore volume (0.04198 cc g^{-1}) and lower band gap energy (2.3 eV), providing a maximum 78.35 mol% FS yield under mild reaction conditions (100 °C and 20 min) with mild energy consumption (12 kJ mL^{-1}). The comparative hydrolysate detoxification study highlighted the superior efficacy of the Amberlite IRP69 cation resin, achieving maximum removal rates of 86% for furfural, 92% for formic acid, and 95% for levulinic acid compared to other methods. Furthermore, the hydrolysate detoxified using Amberlite IRP69 resulted in a higher bioethanol concentration (4.32 mmol mL^{-1}) compared to NaOH neutralization (3.06 mmol mL^{-1}), $Ca(OH)_2$ over-liming (2.88 mmol mL^{-1}), and ethyl acetate solvent extraction (3.73 mmol mL^{-1}) when fermented with *Pichia stipitis*. Additionally, the overall environmental impact assessment indicated that utilizing the Amberlite IRP69 cation resin not only enhanced bioethanol yield but also reduced environmental impacts. Remarkably, the optimized Ga^4Mo-GF catalyst demonstrated reusability for up to 7 cycles in the DCC hydrolysis process, showcasing its stability and the consequential reduction in environmental impacts throughout the corncob to bioethanol conversion process.

Received 5th April 2024,
Accepted 14th August 2024

DOI: 10.1039/d4ya00226a

rsc.li/energy-advances

1. Introduction

The global prevalence of electronic equipment in various industries, coupled with swift technological advancements and intense business competition, results in a significant accumulation of electronic waste. Globally, an amount of 44.7 million metric tons of e-waste was created in 2019, which is expected to reach 74 million metric tons by the year 2030, according to the Global E-waste Monitor-2020.[1] Discarded printed circuit boards (PCBs), the intrinsic components of electronic trash, account for around 3% of e-waste.[2] Hazardous compounds in waste PCBs (W-PCBs), including heavy metals, carcinogenic brominated flame retardants, and polyvinyl chloride, pose a risk to the environment and humans.[3,4] To date, the majority of W-PCBs have been disposed *via* burning and landfilling in India. Therefore, sustainable recycling of W-PCBs is required as accumulation of waste PCBs is not only a quantity problem, but also a serious environmental issue due to the presence of harmful chemicals that pose a threat to occupational, environmental, and human health.

Extraction of precious metals from W-PCBs has been a widespread procedure due to the inherent financial and economic incentives. Very few research works have been reported on recycling of the non-metallic part (NMP) of W-PCBs, comprising 70% of W-PCBs, where the NMP has been used to produce pyrolytic oil,[5] activated carbon,[6] and adsorbents.[7] Recently, a work done by our research group[8] showed that the NMP can be utilized as a promising support to produce a bimetallic catalyst, which was later used for glucose synthesis from jute fiber through a hydrolytic pathway. Notably, glass fiber (GF) constitutes a substantial portion of the NMP, surpassing 50%, and can be effectively employed for producing a

Chemical Engineering Department, Jadavpur University, Kolkata-700032, India. E-mail: rajat_chakraborty25@yahoo.com, rajat.chakraborty@jadavpuruniversity.in; Tel: +91 3324572689

† Electronic supplementary information (ESI) available. See DOI: https://doi.org/10.1039/d4ya00226a

porous support that possess an exceptionally high specific surface area.[9] Thus, in the present study, an effort has been made to synthesize gallium–molybdenum doped glass fiber supported (GaMo–GF) photocatalysts by utilizing W-PCB derived glass fiber (GF).

Utilization of abundant lignocellulosic biomass (LB) to produce bioethanol/biofuel not only is a promising solution for the current energy crisis, but also it helps to mitigate environmental pollution. Corn is amongst the most extensively grown cereal grains, with a 2019 output of 1137 million tons,[10] which generates a large amount of waste corncob. Several studies have utilized corncob as feedstock for biofuel generation due to its high holocellulose (cellulose 32.6 wt% and hemicellulose 31.7 wt%) content.[11] During synthesis of bioethanol from LB, one of the key-steps is synthesis of fermentable sugars through depolymerization of holocellulose. To depolymerize holocellulose, both enzymatic[12] and acid hydrolysis[13,14] procedures are routinely utilized. However, the enzymatic procedure is time-consuming and costly, and the homogeneous acid catalytic route also possesses several bottlenecks, *viz.*, difficulty in product separation, highly corrosive, and waste stream generation. The utilization of heterogeneous catalysts offers a potential solution to the limitations observed in the hydrolysis process using enzymes or mineral acids. For instance, Chen *et al.*, 2019[15] used a rice husk-based solid acid (RH-SO_3H) to produce fermentable sugar from corncob and demonstrated that a maximum 486.53 mg g^{-1} yield of fermentable sugar could be achieved at 160 °C in 3 h. In another study, Wan *et al.*, 2011[16] used sulfated zirconia to hydrolyze corncob hemicellulose and reported that a maximum of 33% (in grams) of soluble sugar can be achieved at 153 °C in 5.3 h. Nonetheless, no work has been reported on corncob hydrolysis to produce fermentable sugar utilizing a GaMo–GF photocatalyst.

For sustainable synthesis of bioethanol from the hydrolysate, it is important to choose a suitable microorganism capable of fermenting both pentose and hexose sugars to bioethanol in an economically feasible way. Although native strains of *Saccharomyces cerevisiae* and *Zymomonas mobilis* are typically employed as benchmark microorganisms in the bioethanol synthesis process,[17] they are unable to ferment pentoses. *Pichia stipitis* has demonstrated considerable potential for industrial utilization among pentose sugar-fermenting yeasts due to its ability to efficiently ferment xylose,[18] as well as a wide range of sugars, resulting in a high bioethanol yield.

In bioethanol production from lignocellulose, fermentation inhibition can be addressed by detoxifying the hydrolysate before fermentation. Among various detoxification methods, ion-exchange resin treatment proved to be one of the most effective methods. For instance, a study conducted by Villarreal *et al.*, 2006[19] reported that an ion exchange resin is more efficient than activated charcoal and drastically enhances the fermentability of the hydrolysate. Similar results were obtained by Chandel *et al.*, 2007[20] in the detoxification of the sugarcane bagasse hydrolysate employing an ion-exchange resin, where it was reported that an ion-exchange resin can significantly reduce phenolic components by 75.8% and furan components by 63.4%.

Over the decades, a significant amount of research has been conducted on bioethanol production from lignocellulosic biomass (LB) through enzymatic hydrolysis followed by fermentation.[21] However, there is a scarcity of studies focusing on bioethanol production *via* hydrolysis of LB using chemical catalysts and subsequent fermentation. Recently, Selvakumar *et al.*, 2022[22] used a binary liquid acid (H_2SO_4 and CH_3COOH) to hydrolyse corncob and performed the fermentation process using *Saccharomyces cerevisiae* resulting in a maximum bioethanol concentration of 24.6 mg mL^{-1}. In another work, Yücel *et al.*, 2015[23] used H_2SO_4 to hydrolyse sugar beet pulp to produce a hemicellulose hydrolysate, which was then fermented by *Pichia stipitis* to produce bioethanol. Nonetheless, no work has been reported yet on bioethanol production through hydrolysis of LB using a solid acid catalyst to the best of our knowledge.

Over the last few decades, the increasing problem of environmental pollution has spurred researchers to revise existing chemical practices, seeking to establish more sustainable systems. In this context, life-cycle assessment (LCA) analysis emerges as a valuable tool for identifying efficient processing and energy systems in the process industries. Recently, several LCA studies on corncob based lignocellulosic biorefinery systems for bioethanol production have been reported.[24,25] For instance, Banerjee *et al.*, 2023[26] performed a comparative life cycle assessment study of biological and chemical lignocellulose pretreatment and downstream processing for conversion of lignocellulose to biofuel. However, based on the analysis of existing literature reviews, it is observed that conducting a comparative life-cycle assessment (LCA) analysis of various detoxification steps is necessary to determine the most environmentally sustainable and efficient approach.

Thus, the current research focuses on developing a cost-effective W-PCB derived glass fiber supported gallium–molybdenum (GaMo–GF) photo-catalyst for synthesis of fermentable sugar from corncob followed by production of bioethanol through fermentation using *Pichia stipitis*. First, the GaMo–GF catalyzed corncob hydrolysis process was optimized in a quartz halogen solar irradiation (QHS) assisted batch reactor (QHSR). Afterwards, the produced hydrolysate was detoxified and subsequently fermented in an Erlenmeyer flask at 30 °C under shaking conditions. Finally, a life-cycle assessment (LCA) analysis was carried out, which included evaluation of environmental consequences and sustainability of each process step.

2. Results and discussion

2.1. Hydrolysis of DCC under optimal conditions

Table 1 displays the rankings of four process parameters, according to their delta (δ) acquired from the experimental designs and the L-9 TgOD projected values. The greater the value of δ, the higher the rank. It can be seen from the table that the reaction temperature (R_T) plays the most significant role in the photo-hydrolysis of corn cob closely followed by the catalyst concentration (C_c). Furthermore, ANOVA analysis

Table 1 SN ratio and delta values for GaMo–GF catalysed photohydrolysis of corncob

Level	Temperature (R_T) (°C)	Time (R_t) (min)	Catalyst concentration (C_c) (wt%)	Ga precursor loading (P_L) (wt%)
L_{-1}	31.80	33.40	32.39	32.81
L_0	35.22	34.56[a]	34.16	34.98[a]
L_{+1}	35.38[a]	34.44	35.85[a]	34.62
Delta (δ)	3.55	1.20	3.31	1.88
Rank	1	4	2	3

[a] Optimum level of the process parameter.

(Table S1, ESI†) for the photocatalytic corncob hydrolysis process confirmed that R_T and C_c were statistically important process parameters at the 95% confidence level (p-value $<$ 0.05). On the other hand, the highest SN values indicate the process factor's optimum level. Accordingly, from Table 1 it can be deduced that L_{+1} of R_T (100 °C), L_{+1} of C_C (15 wt%), L_0 of P_L (4 wt%) and L_0 of R_t (30 min) were the optimum process values. Finally, under optimized process conditions, the DCC photohydrolysis run yielded a maximum of 78.35 mol% FS, which contained 51.65 mol% glucose and 26.7 mol% xylose.

2.2. Interactive impacts of process factors on DCC hydrolysis

Fig. 1 depicts the effects of individual process factors (in terms of the SN ratio) and their parametric interactions on FS yield in the corncob hydrolysis process. Fig. 1(a) illustrates that as the temperature rises from 80 °C to 90 °C (keeping other factors constant), there is a notable increase in the SN ratio, indicating a greater yield of FS. However, as the temperature continues to increase beyond this point, the SN ratio remains relatively constant. This could be attributed to the onset of FS degradation at higher temperatures, thereby limiting further enhancement of the SN ratio. Similarly, for reaction time after 30 min the product be might further degraded, which reduces the SN ratio. Upon increasing the precursor loading (P_L) from 2 wt% to 4 wt% the surface acidity and the photocatalytic effect increase, hence the SN ratio or FS yield increases. But, a further increase in P_L has a negative impact on the FS yield. Above 4 wt%, the enlarged nanoparticle size blocked the GF support's pore, reducing the catalyst's total surface area dramatically (BET and XRD analyses). Notably, a comparative study was undertaken to assess the impact of utilizing an optimized Ga[4]Mo-GF photocatalyst *versus* a GaMo catalyst without the GF support on the DCC hydrolysis process, aiming to determine whether the GF support impeded or improved the process. Interestingly, the GaMo catalyst without the GF support exhibited a lower FS yield (55.4 mol%) in comparison to Ga[4]Mo–GF, possibly attributable to the presence of Brønsted acidic sites within the GF structure. Moreover, from Fig. 1(a), it was observed that the FS yield increases linearly with the catalyst concentration, indicating that the availability of more active sites for the reaction contributes to this phenomenon.

From the interaction plot of catalyst concentration *vs.* temperature (Fig. 1(b)), it can be seen that while keeping all other parameters constant, with an increase in catalyst concentration at all temperatures the yield of FS increased. This exemplified how the created GaMo–GF catalyst significantly facilitated the DCC hydrolysis process. A similar pattern was seen for all reaction time levels. At the same time, the catalyst concentration *vs.* gallium precursor loading plot revealed that increasing the gallium loading at a low concentration increased the FS yield. In contrast, at higher catalyst concentration, the FS yield increases until the gallium loading is 4 wt%. Then it decreases due to the decrease in surface area and creation of bigger nanoparticles during catalyst preparation with increased precursor loading. Moreover, the temperature *vs.* time graph reveals that at high temperatures, the FS yield decreases as time increases because of the degradation of FS.

2.3. GaMo–GF catalyst characterization

2.3.1. X-ray diffraction patterns. The X-ray diffraction (XRD) patterns of glass fiber powder and GaMo–GF photocatalysts are shown in Fig. 2. Peaks corresponding to the crystalline phase of molybdenum trioxide (33.15°, 49.48°, and 55.22°),[27] gallium oxynitrate (26.62° and 58.04°),[28,29] β-gallium oxide (47.56° and 77.2°), silicon-oxide (22.8°)[30] and aluminum-silicon oxide (18.64° and 28.72°)[31] have been observed for all catalysts as shown by plots A, B, and C. The presence of silicon in the GF powder is demonstrated by a hump as shown in the

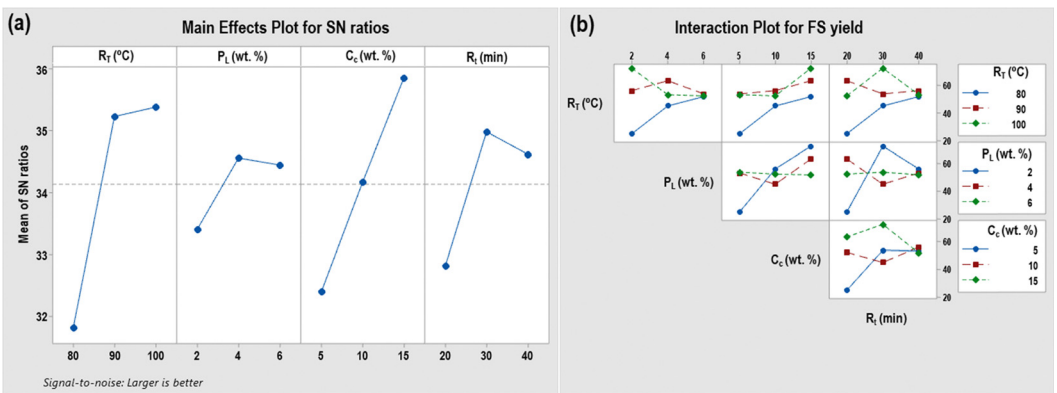

Fig. 1 (a) Main effects plot for SN ratios and (b) interaction plot for FS yield.

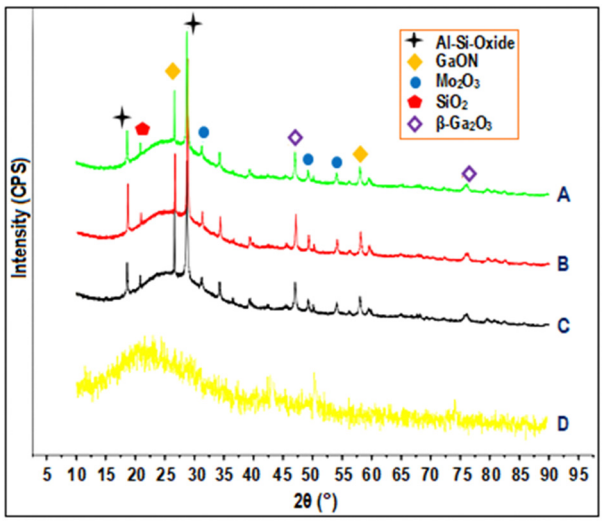

Fig. 2 XRD patterns of (A) Ga^6Mo–GF, (B) Ga^4Mo–GF, (C) Ga^2Mo–GF and (D) GF.

figure, which is attributable to the presence of SiO_2 across all catalysts.[32] It can be concluded from the figure that as the gallium loading is increased the peak intensity of gallium oxynitrate also increases. The sample's crystallite size (D_c) was determined using the Debye–Scherrer equation (eqn (1)):

$$D_c = \frac{0.9\lambda}{\beta \cos\theta} \quad (1)$$

where λ is the X-ray beam's wavelength (λ = 1.5147 Å), β is the intense peak's full width at half maximum (FWHM), and θ is Bragg's angle. Using the above equation, the crystallite sizes of MoO_3, GaON and β-Ga_2O_3 are found to be 6.97, 20 and 15.54 nm respectively.

2.3.2. NH_3-TPD analysis. NH_3-TPD analysis conducted on the GaMo–GF photocatalysts (as shown in Fig. 3) indicated the presence of both weak (with signal maxima at 175–225 °C) and strong (with signal maxima at 325–375 °C) acidic sites on the surface of each photocatalyst across the temperature range of 100–550 °C. Additionally, it was possible to see that the NH_3 desorption peak was enhanced in the higher temperature zone with an increase in gallium precursor loading, while showing lower peaks in the lower temperature zone, which is in accordance with previous studies.[33] For instance, in Fig. 3, a slight increase of 2 wt% in gallium precursor loading in Ga^2MO-GF resulted in 9.2% enhancement of the NH_3 desorption peak in the higher temperature zone (for Ga^4MO-GF), while the peaks in the lower temperature zone were reduced to 4%. This was due to the partial replacement of aluminium with gallium, which increases the Lewis acid sites (high-temperature zone). Moreover, as depicted in Fig. 3, low-temperature weak acid sites were also present in all the prepared catalysts, which enhanced the FS yield.

2.3.3. Fourier transform infrared (FTIR) spectroscopy analysis. The FTIR spectra of optimum the Ga^4Mo–GF catalyst is depicted in Fig. 4. FTIR studies of the optimum catalyst revealed a peak at 3748.82 cm^{-1} owing to the existence of absorbed water with a significant OH stretching mode.[34] The broad peak at 2999.97 cm^{-1} and 2805.36 cm^{-1} corresponds to the C–H stretching vibrations.[35] Sharp peaks near 2274.42 cm^{-1} indicated the presence of C–N stretching modes in the produced catalysts.[36] The peak at 1508.2 cm^{-1} indicates the presence of a nitro compound, which can be confirmed from XRD data to be GaON. Furthermore, the catalyst spectra showed peaks at 764.22 cm^{-1} and 463.1 cm^{-1}, which were related to vibration of Ga–O.[37] The presence of Si–O[38] is evident from the peak at 1084.4 cm^{-1} and 811.24 cm^{-1}. Additionally, characteristic peaks at 996.52 cm^{-1} and 605.27 cm^{-1} might be ascribed to Mo–O bonds.

2.3.4. Thermo-gravimetric analysis (TGA). TGA of GF and the optimum Ga^4Mo–GF photocatalyst was carried out to establish the materials' thermal stability when heated over a wide range of temperatures, ranging from 30 to 780 °C, as shown in Fig. 5. At 270–370 °C, the TGA thermogram of GF indicates a significant weight loss (31%), which is attributed to the degradation of un-extracted epoxy resin. The GF thermogram further reveals a weight loss of 15% from 400 to 650 °C, which was attributed to the oxidation of the solid residue generated during the first decomposition step.[39] The weight % *vs.* temperature graph of Ga^4Mo–GF shows a sharp weight loss of 10% in the temperature range of 110–200 °C; evaporation of adsorbed water is most likely to be responsible for the

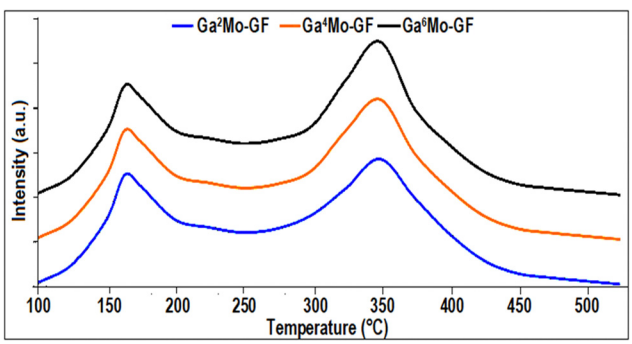

Fig. 3 NH_3-TPD of the synthesized GaMo–GF photocatalysts.

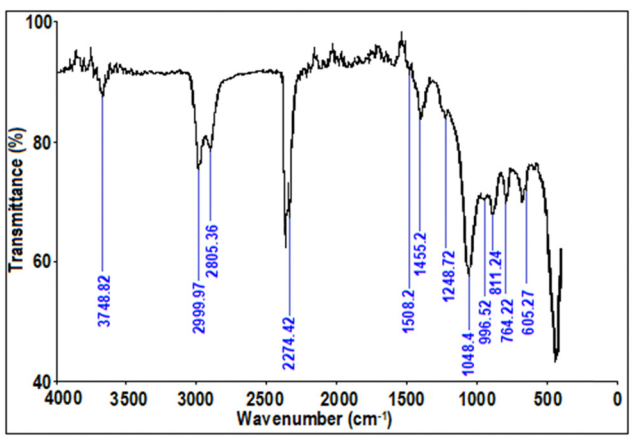

Fig. 4 FTIR spectra of the Ga^4Mo–GF photocatalyst.

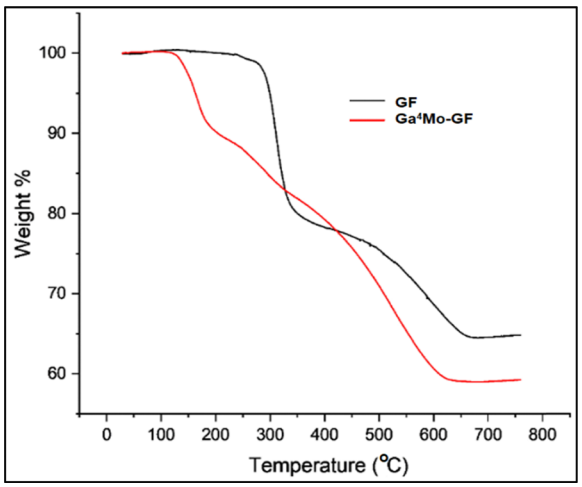

Fig. 5 TGA of GF and the Ga^4Mo–GF photocatalyst.

occurrence of this behavior. Furthermore, from 200 °C to 450 °C, there is a progressive 13.5% weight loss due to the decomposition of the gallium precursor to gallium oxides.[40] There is a further weight loss of about 17% from 450 °C to 650 °C, which is due to the formation of MoO_3 from the molybdenum precursor.[41] As a result, all the prepared catalysts were calcined in a muffle furnace for two hours at 700 °C to improve thermal stability. Since the photo-degradation of DCC has been performed below 100 °C (well below 650 °C), the thermal degradation of catalysts was highly improbable.

2.3.5. UV-vis-NIR spectroscopy analysis. The UV-vis-NIR spectrophotometric measurement (Fig. 6(a)) of the optimal Ga^4Mo–GF catalyst revealed a sharp absorbance peak in the wavelength range of 400–550 nm (in the visible light range), showing the existence of GaON[42] in the generated photocatalyst. The margins of the absorption bands between 400 and 550 nm show that visible light may excite electrons in Ga^4Mo–GF to move from the valence band to the conduction band. Using the Kubelka–Munk equation and the Tauc plot, a band gap energy (E_g) of 2.3 eV of GaMo–GF was calculated from reflectance spectra (Fig. 6(b)). Interestingly, there was no absorbance peak in the 600–800 nm wavelength range, which indicates the complete extraction of copper[43] by a acetic acid treated copper removal process.

Table 2 BET analysis of the GF support and Ga^4Mo–GF photocatalyst

Sample	Surface area ($m^2\ g^{-1}$)	Total pore volume (cc g^{-1})	Pore diameter (nm)
GF support	20.35	0.03	11.90
Ga^4Mo-GF	28.01	0.04	13.59

2.3.6. Brunauer–Emmett–Teller (BET) analysis. The specific surface areas of the optimum Ga^4Mo–GF photocatalyst and the W-PCB derived GF were determined using Brunauer–Emmett–Teller (BET) analysis (Table 2). After calcination, the optimum Ga^4Mo–GF catalyst had a surface area of 28.01 $m^2\ g^{-1}$, which is much greater than that of a W-PCB-derived silica–alumina support (20.25 $m^2\ g^{-1}$). During the calcination process, a significant portion of the oxides, nitrates, and organic matter undergo evaporation (observed in TGA analysis), leading to the formation of numerous pores. This phenomenon causes an expansion in the surface area of the photo-catalyst. BET analysis of optimum Ga^4Mo–GF (Fig. 7) reveals that the isotherm is convex to the (P/P_0) axis, which can be described as type III of the IUPAC classification based on the form of the isotherm. Besides, the total pore volume and pore diameter data showed that the Ga^4Mo–GF photocatalyst is mesoporous in nature, which can easily adsorb the reactants during the photocatalytic DCC hydrolysis reaction.

2.3.7. X-ray photoelectron spectroscopic (XPS) analysis. XPS examination showed the electronic states of the component species of the Taguchi derived optimal photocatalyst in Fig. 8. The two peaks at 233.4 eV and 236.2 eV, corresponding to Mo $3d_{5/2}$ and Mo $3d_{3/2}$,[44] respectively, indicated that the Mo species was present as MoO_3 in the photocatalyst. The peak of gallium at 19.97 eV and 24.01 eV corresponds to the presence of GaON.[42] As illustrated in Fig. 8, Si 2p shows two peaks, the peak at 103.5 eV indicates the Si–O bonds and the peak at 102 eV is ascribed to the Al–O–Si bridge of the GF structure, which can be well supported by FTIR studies, and the binding energy of

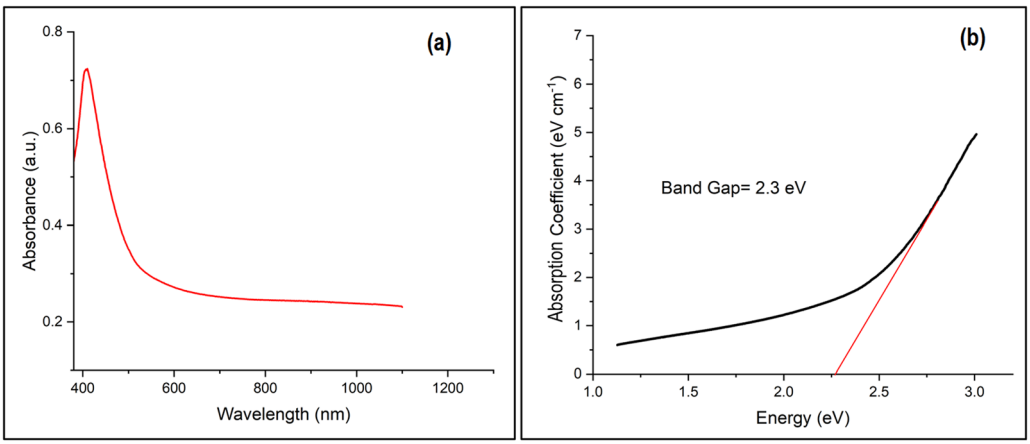

Fig. 6 (a) Absorbance spectra and (b) Tauc plot of the optimal catalyst (Ga^4Mo–GF).

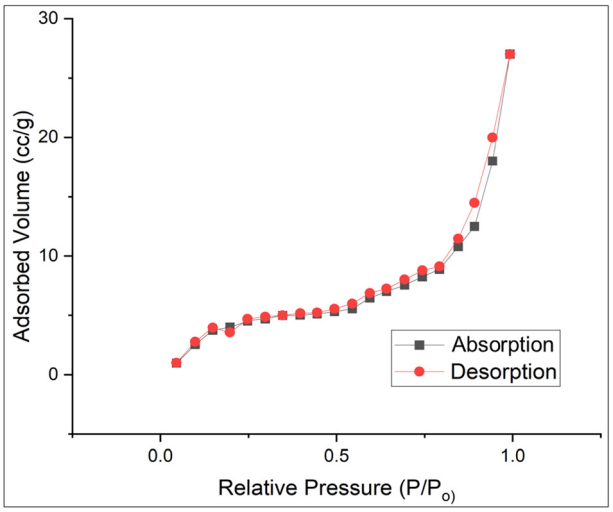

Fig. 7 BET isotherm of the optimum Ga^{4}Mo–GF catalyst.

Al (= 74.4 eV) is a more credible sign of aluminosilicate presence. Notably, the two peaks at 347.18 eV and 351.02 eV correspond to Ca $2p_{3/2}$[45] present in the GF structure, which is well supported by EDAX analysis (shown in Fig. 9(d)).

2.3.8. Scanning electron microscopy (FESEM) and EDAX analyses. The surface morphology of the untreated W-PCB powder (Fig. 9(a)), treated W-PCB (Fig. 9(b)) and GF supported optimum GaMo–GF photocatalyst (Fig. 9(c)) was revealed by FESEM analysis at various magnifications. The untreated W-PCB powder sample's morphology as seen in Fig. 9(a) depicts fiber glass rods encased in the epoxy resin in an uneven rod form. After treatment, the epoxy resin on the fiber glass rod was reduced and exposed the surface of the GF (Fig. 9(b)), which in turn enhanced the surface area (revealed from BET analysis). Fig. 9(c) depicts MoO_3 and GaON grafted on the GF support of the optimum GaMo–GF catalyst. Moreover, the EDAX analysis of the optimal photocatalyst showed normalized weight percentages of aluminum, silica, and calcium (main elements of GF), alongside gallium and molybdenum (Fig. 9(d)).

2.3.9. HRTEM analysis. HRTEM analysis was carried out in order to understand the structure better as seen in Fig. 10. ImageJ software has been used to measure the impregnated metal crystallite sizes, which confirms the nano-impregnation of MoO_3 and GaON on the GF support. The measured crystallite sizes of MoO_3 and GaON were 7.24 and 22.147 nm respectively, which is further confirmed from the calculated XRD data. The *d*-spacing of the catalyst has also been evaluated. As seen from Fig. 10 (c), the *d*-spacing of 0.328 nm confirms the (110 plane) of the orthorhombic MoO_3 phase[46] and 0.475 nm corresponds to the *d*-spacing of gallium.[47]

2.4. Comparative analysis with pertinent prior research

A comparison of current research with previously published studies on FS synthesis employing a heterogeneous solid catalyst has been conducted and is presented in Table 3. It has been observed that production of fermentable sugars from cellulose or other biomasses mostly requires severe reaction conditions. Though use of microwave (MW) irradiation (1200 W)[48,49] gives higher yield under less severe reaction conditions, the energy consumption is very high. On the other hand, in the present study, photocatalytic hydrolysis of DCC under quartz halogen radiation (200 W) has milder reaction conditions, comparatively higher FS yield (78.35 mol% and selectivity: 81.57%) and consumes a much less energy (12 kJ mL^{-1}). Notably, the optimum catalyst provided a similar 40.70 mol% FS yield (selectivity: 74.32%) under conventional heating and mild optimum reaction conditions while still consuming less energy (24 kJ mL^{-1}) compared to the previously

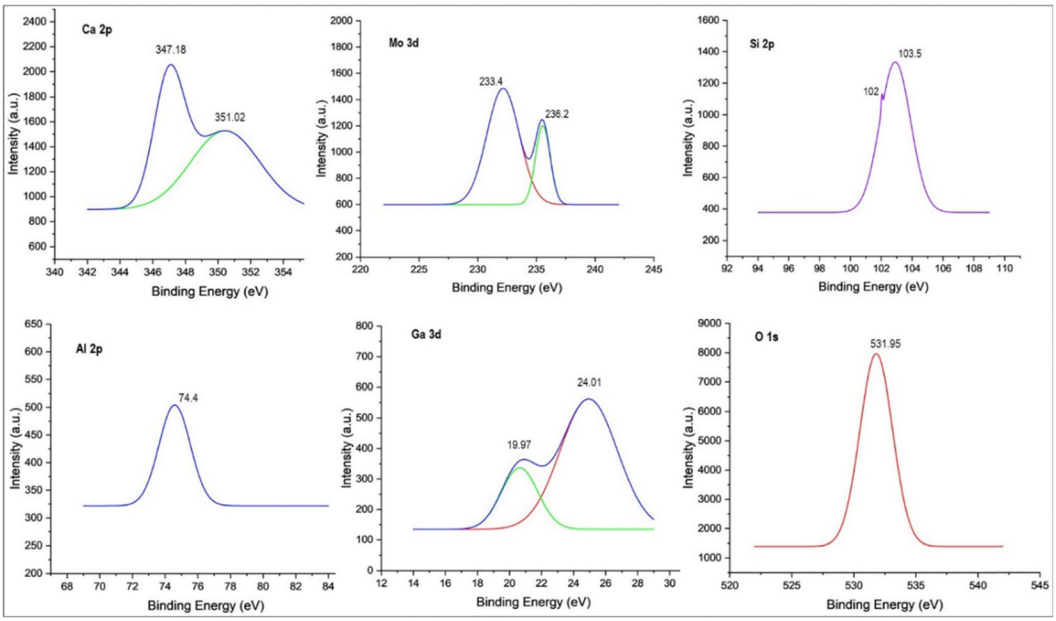

Fig. 8 XPS of the optimum Ga^{4}Mo–GF catalyst.

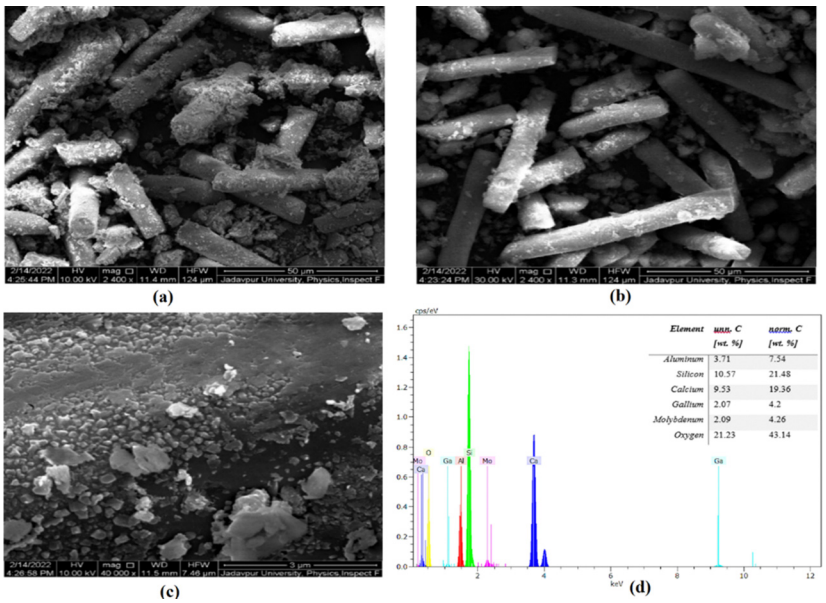

Fig. 9 FESEM images of (a) the GF support, (b) & (c) optimum Ga^{4}Mo–GF, and (d) EDAX analysis of Ga^{4}Mo–GF.

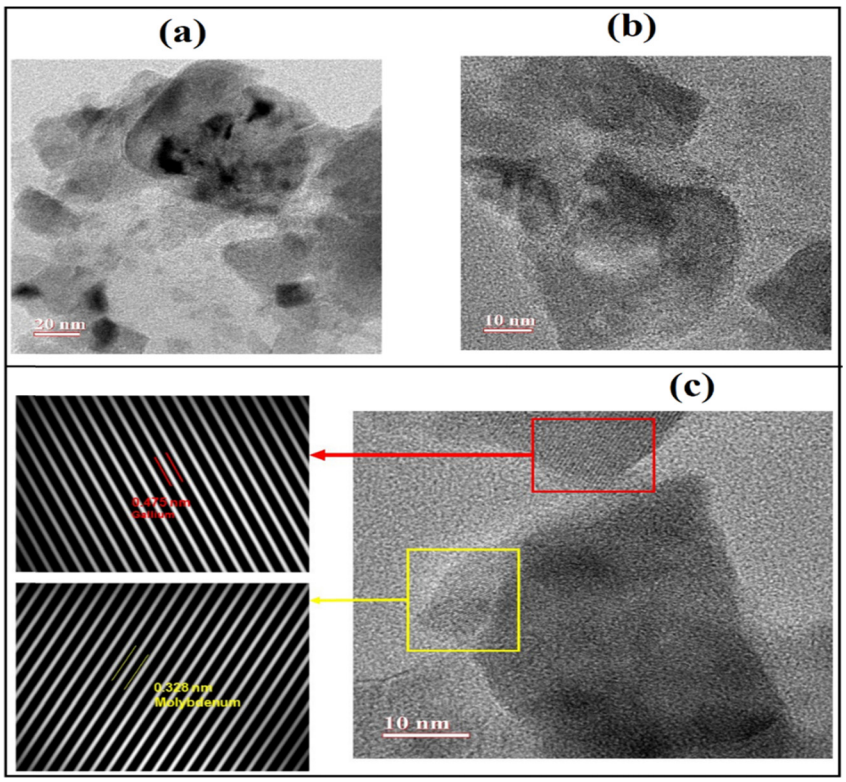

Fig. 10 HRTEM image of the Ga^{4}Mo–GF photocatalyst.

reported study.[48,49] Additionally, a cost analysis study revealed that the estimated cost of the W-PCB derived GF is significantly lower (INR 37.63 per kg) compared to the commercial silica-alumina cost (INR 475 per kg (www.indiamart.com)), which not only reduces the preparation cost of 1 kg of the Ga^{4}Mo–GF photocatalyst but also enhnaces catalyst performance in terms of FS yield. Therefore, in the present study, the photocatalytic conversion process of corncob in the QHSR using the Ga^{4}Mo–GF catalyst emerges as a potentially more sustainable approach compared to those reported in previous works.

Table 3 Comparative study on FS production

Feedstock	Catalyst	Reaction conditions	Reactor	Yield (%)	Ref.
Cellulose	BC–SO_3H	90 °C; 1 h	MW[a] heated batch reactor	24.1	48
Cellulose	[C_4mim]Cl + HY	100 °C; 0.25 h	MW heated batch reactor	34.8	49
Cellulose	[C_4mim]Cl + HZSM	100 °C; 0.167 h	MW heated batch reactor	42.9	
Cellulose	Au-HYT	140 °C; 16 h	VIS[b] enegized batch reactor	58.7	50
Corncob	CSA	130 °C; 1 h	MW heated batch reactor	34.6	51
Cellulose	CP-SO_3H	120 °C; 10 h	Conventionally heated batch reactor	91	52
Cellulose	[BMIm]Cl + HY	130 °C; 0.5 h	Conventionally heated batch reactor	68.2	53
DCC	GaMo–GF	100 °C; 0.5 h (30 min)	QHSR	78.35	Present study

[a] Microwaves. [b] Visible light.

Table 4 Composition of detoxified DCC hydrolysates

Detoxification method	Component concentration in hydrolysates (mmol mL^{-1})						Total sugar loss (mmol mL^{-1})
	Glucose	Xylose	Formic acid	Furfural	Levulinic acid	5-HMF	
None	3.43	1.41	0.493	0.27	0.33	0.104	0
Neutralization with NaOH (pH: 6.5–7.00)	3.27	1.10	0.092	0.23	0.23	0.077	0.462
Over-liming with $Ca(OH)_2$ (pH: 10)	3.12	0.95	0.192	0.138	0.0925	0.077	0.771
Ethyl acetate extraction	3.39	1.35	0.32	0.10	0.192	0.023	0.10
Amberlite IRP69 resin	3.39	1.34	0.0385	0.0385	0.0154	0	0.11

2.5. Detoxification and fermentation of DCC hydrolysates

Detoxification results of the Taguchi derived optimal DCC hydrolysates using various detoxification approaches are shown in Table 4. From Table 4, it can be clearly observed that the minimum sugar loss was observed for the ethyl acetate solvent extraction detoxification process and the cation exchange detoxification process using the Amberlite IRP69 resin. Notably, the maximum removal of inhibitors, *viz.*, furfural (86%), formic acid (92%), and levulinic acid (95%), can be achieved using the Amberlite IRP69 cation resin compared to other detoxification methods. Although the ion exchange detoxification process may have a higher initial cost due to the high price of the Amberlite IRP69 cation resin, its easy recyclability mitigates the significance of the price factor when choosing an appropriate detoxification method.

Fig. 11 demonstrates the correlation between total fermentable sugar (FS), glucose, and xylose consumption with bioethanol production during the fermentation process of the Amberlite IRP69 resin detoxified DCC hydrolysate. The findings indicated a substantial rise in bioethanol concentration from 0 to 80 hours, followed by deceleration of the *Pichia stipitis* NCIM 3499 strain approaching the stationary phase with limited available fermentable sugar being present in the substrate. The maximum bioethanol concentration of 4.32 mmol mL^{-1} was observed after completion of the fermentation period of 120 h. The fermentation process also yields some by-products, with xylitol being the primary one (1.21 mmol mL^{-1}).[54] Although acetic acid is also produced,[55] its concentration remains relatively low (<0.1 mmol mL^{-1}). Notably, xylitol has various applications in the pharmaceutical and food industries, and its demand is currently increasing. Therefore, integrated production of ethanol and xylitol could be a sustainable process from a techno-economic perspective.

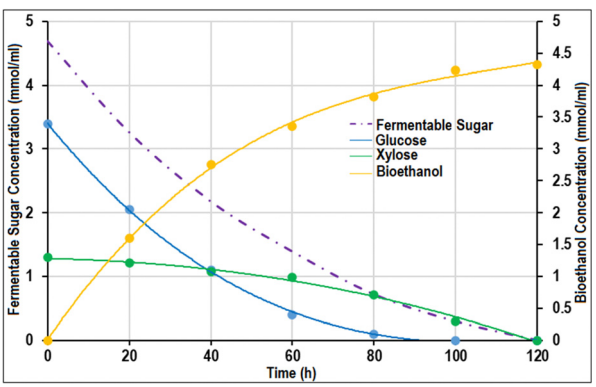

Fig. 11 Changes in fermentable sugar (FS), glucose, xylose and bioethanol concentration with time in the Amberlite IRP69 resin detoxified hydrolysate fermentation process.

The fermentation study was also conducted using other detoxified DCC hydrolysates under identical operating conditions. The results demonstrated that when using NaOH neutralized, Ca $(OH)_2$ over-limed and ethyl acetate solvent extracted detoxified hydrolysates, maximum bioethanol concentrations of 3.06 mmol mL^{-1}, 2.88 mmol mL^{-1}, and 3.73 mmol mL^{-1} were achieved, respectively. The findings of this study showed that the Ga^4Mo–GF photocatalytic hydrolysis in conjunction with the detoxification method using the Amberlite IRP69 resin was a promising option for successful DCC conversion into sugars and bioethanol.

While no prior research has addressed lignocellulosic biomass hydrolysis utilizing heterogeneous solid catalysts followed by fermentation for ethanol production, certain studies have explored lignocellulosic biomass hydrolysis with homogeneous catalysts followed by fermentation. For instance, Selvakumar *et al.*, 2022[22] utilized a binary liquid acid (H_2SO_4 and CH_3COOH) to hydrolyze corncob at 120 °C for 60 minutes, achieving a maximum

bioethanol concentration of 24.6 mg mL^{-1} h^{-1} through fermentation employing *Saccharomyces cerevisiae*. The ethanol concentration obtained in their study was significantly lower compared to the present work (99.58 mg mL^{-1} h^{-1}), and their approach involved the use of corrosive liquid acids during the hydrolysis process, which are challenging to separate and render the process energy-intensive. In another study, Yücel *et al.*, 2015[23] utilized H_2SO_4 to hydrolyze sugar beet pulp, generating a hemicellulose hydrolysate and the hydrolysate was detoxified through methods involving activated charcoal obtained from sugar beet pulp and over-liming with CaO. The work also reported that the detoxified hydrolysate when fermented by *Pichia stipitis* yielded a maximum ethanol concentration ranging from 10.8 to 12.2 mg mL^{-1}, which was lower compared to the ethanol obtained from the Amberlite IRP69 resin detoxified DCC hydrolysate in the present study. Notably, a fermentation experiment was also conducted on a non-detoxified hydrolysate and only 1.56 mmol mL^{-1} of ethanol concentration was observed after completion of the fermentation period of 120 h. Although the cost of the Amberlite IRP69 resin is high, it significantly increases ethanol yield (63.8% higher) from a detoxified hydrolysate compared to a non-detoxified hydrolysate. Consequently, the present investigation into DCC hydrolysis utilizing Ga^4Mo–GF, subsequent detoxification with the Amberlite IRP69 resin, and fermentation employing *Pichia stipitis*, highlights its economic viability.

Although 1G bioethanol production is commercially established, 2G bioethanol processes are still immature and costly, due to the lack of robust technology, posing major challenges to commercial viability. Notably, 1G feedstocks like sugarcane juice compete with food production, whereas 2G feedstocks such as waste sugarcane residues, rice straw and corn stover are abundant and do not compete with food resources. Additionally, lignocellulosic biomass (LB) can produce up to 50% more ethanol when integrated with 1G refineries;[56] thus, the integrated process for production of 1G and 2G bioethanol can significantly enhance global ethanol yields. For instance, a study on 2G bioethanol production conducted by Vikash *et al.*, 2018[57] utilizing sugarcane and trash obtained from a sugar mill in India reported that the break-even selling price of bioethanol was $$1.05 per L, which is higher than the current production cost of 1G bioethanol from sugarcane ($$0.56 per L). On the other hand, another study conducted by Macrelli *et al.*, 2012[58] reported that the minimum selling price of 2G bioethanol produced from sugarcane bagasse was $$0.97 per L, whereas the overall production cost of 1G + 2G bioethanol would be about $$0.40 per L with an output of 102 L per ton dry sugar cane. The study also reported that the enzymatic hydrolysis process has the highest impact on the overall cost of bioethanol.

Despite the current process involving multiple steps for SB to 2G bioethanol production, the use of low-cost, waste-derived recyclable solid acid catalysts (preparation cost < $1 per kg) instead of expensive commercial enzymes (cellulase, price: $50–55 per kg, www.echemi.com) in the saccharification steps significantly reduces overall operational costs. Additionally, the detoxification steps using the Amberlite IRP69 resin generate several value-added by-products, such as formic acid, levulinic acid, 5-HMF, and furfural. If these by-products are appropriately purified, they can contribute to making the overall process economically sustainable. The lignin generated during the SB pretreatment process can also be utilized to produce value-added chemicals. Furthermore, the co-production of value-added chemicals like xylitol during the fermentation of the hydrolysate, alongside ethanol, can further help to reduce the production cost of ethanol. A preliminary techno-economic cost analysis of the current bioethanol production process indicates that the production cost is $0.72 per L without factoring in value-added by-products. However, with the inclusion of by-products such as xylitol ($4–5 per kg, **https://www.echemi.com**), levulinic acid ($0.1 per kg, **https://www.echemi.com**), 5-HMF ($25 per kg, **https://www.echemi.com**), and furfural ($0.2–0.3 per kg, **https://www.echemi.com**), the cost drops to about $0.52 per L, which can be lower or comparable with the production cost of 1 G bioethanol from sugarcane.

2.6. Life-cycle impact assessment

The results of the environmental impact assessment utilizing ReCiPe Midpoint (H) v1.11 are depicted in Fig. 12 and 13. Fig. 12 shows that the potential midpoint environmental impact indicators for the corncorb to bioethanol production process, comparing all four system borders, were climate change, fossil depletion, human toxicity, metal depletion, and water depletion. Moreover, in the detoxification process of DCC hydrolysates, both Amberlite IRP69 resin extraction and ethyl acetate extraction processes exhibit lower environmental impacts across all potential midpoint indicators compared to the other two detoxification techniques (Fig. 13). Remarkably, the bioethanol production from the Amberlite IRP69 resin-extracted DCC hydrolysate shows reduced environmental impacts across all categories, excluding the human toxicity indicator, in comparison to bioethanol production from the ethyl acetate-extracted DCC hydrolysate.

Fig. 13 depicts the individual process contributions to the potential impact indicators of overall environmental impacts, highlighting that the GaMo–GF catalyst preparation and corncorb delignification processes were the primary contributors among all processes. Molybdenite and gallium mine operations for the preparation of molybdenum and gallium precursor salts (40–63%), trailed by coal-based electricity and NaOH utilization (36%) during W-PCB treatment, emerged as the major contributors to environmental impact indicators such as metal depletion (96.6%) and human toxicity (92.7%) for the GaMo–GF catalyst preparation process. On the contrary, concerning the corncob delignification process, notable factors contributing to impact indicators such as fossil depletion and climate change included the consumption of acetic acid (25.20–29.63%) and the electricity used during corncob grinding (2.42–3.65%).

Notably, a catalyst recycling study of the DCC hydrolysis process revealed that the prepared optimized catalyst Ga^4Mo–GF could be utilized up to 7 cycles without compromising the FS yield. During this study, ICP-MS analysis was conducted after each hydrolysis cycle, which revealed that a marginal leaching of Ga (1.5 ppm) and Mo (2.14 ppm) metal elements

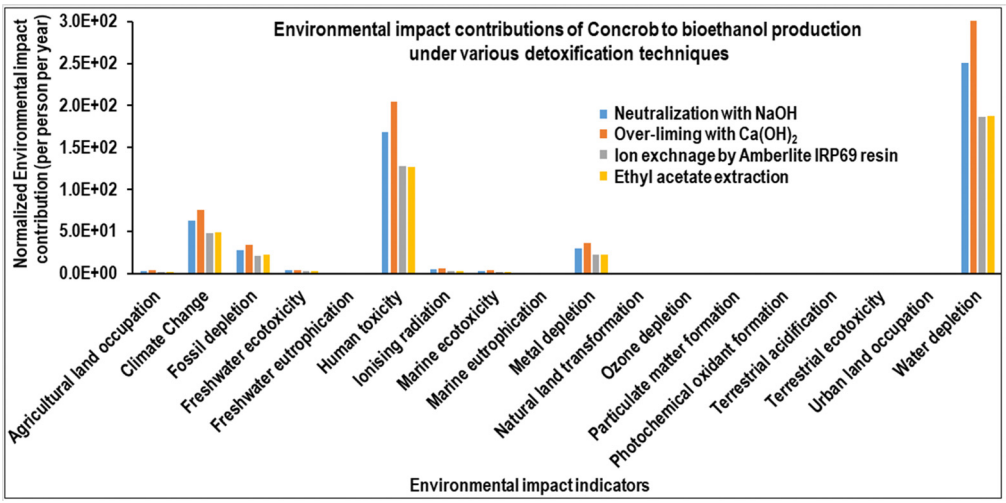

Fig. 12 Environmental impact analysis of the corncob to bioethanol production process.

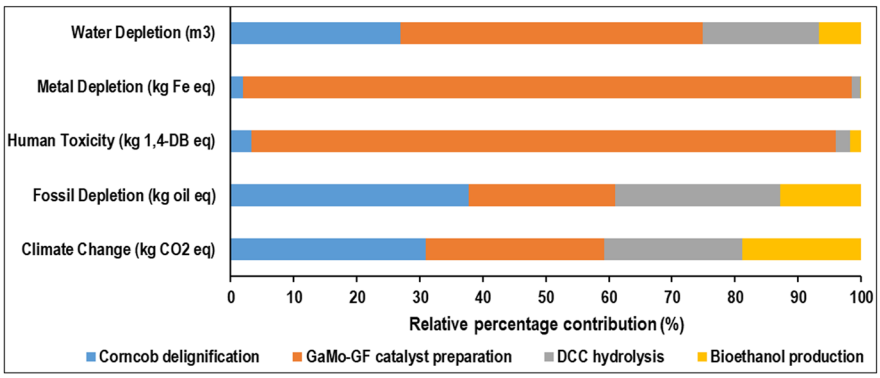

Fig. 13 Individual process contributions to the overall environmental impacts.

occurred after the seventh cycle. A comparative life cycle impact assessment conducted on the DCC hydrolysis process utilizing both fresh and reused Ga^4Mo-GF catalysts (Fig. 14) indicated that employing the reused catalyst could lead to significant reduction in major midpoint indicators, including climate change, fossil depletion, human toxicity, metal depletion, and water depletion, by 85%, 86%, 36.4%, 85.7%, and 49%, respectively, compared to the fresh catalyst.

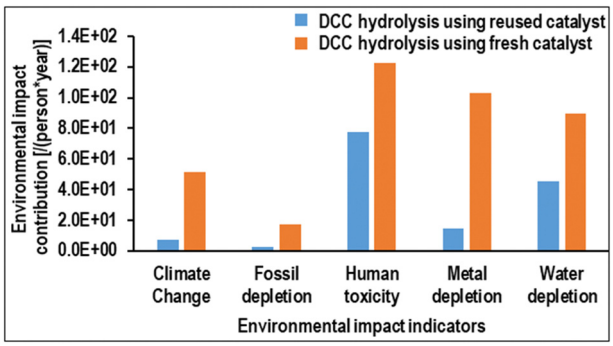

Fig. 14 Comparative environmental impact assessment of the DCC hydrolysis process employing reused and fresh Ga^4Mo–GF catalysts.

3. Experimental procedure

3.1. Materials

W-PCBs were obtained for this study from a regional scrap store in Kolkata, West Bengal, India. Corn cob has been collected from local vendors in Kolkata, West Bengal, India. Transition metallic salts, *viz.*, gallium(III) nitrate hydrate and bis(acetylacetonate) dioxo-molybdenum(VI), have been purchased from Sigma-Aldrich. H_2O_2 (30% w/w), acetone (>99%), acetic acid (CH_3COOH, 99–100%), NaOH, Ca $(OH)_2$, NH_4OH solution (25% w/w), Amberlite IRP69 resin, and *N*,*N*-dimethylformamide (DMF) of analytical grade have been procured from Sigma-Aldrich. The *Pichia stipitis* NCIM 3499 strain was collected from the National Collection of Industrial Microorganism (NCIM), Pune, India.

3.2. Catalyst preparation using a W-PCB derived glass fiber (GF) support

3.2.1. Glass fiber (GF) support preparation. The collected W-PCBs were first washed with hot water and all the

unnecessary elements (conductive rails, RAMs, slots *etc.*) were disassembled and physically removed. As per Moyo *et al.*, 2020,[59] the W-PCBs were then cut into pieces of 5 cm × 5 cm and the pieces were then immersed in 10 M NaOH for 24 hours without agitation before being washed in water. As a result, the remaining metal alloys were delaminated from the surface and the surface coating along with some inner epoxy resin was removed, revealing the copper clad. The W-PCBs were then ground in an ultrafine grinder, *i.e.*, a drum sander, and passed through an ASTM 45 mesh (~355 μm). The ferrous elements in W-PCBs were then removed by employing a wet magnetic stirrer (100 W) for 0.5 h. Sedimentation partly eliminated the remaining heavy particles such as tin, aluminum, zinc, and lead. After this, the resulting combination of glass fiber, copper, and other materials was washed and collected by filtering. Then, DMF (*N*,*N*-dimethylformamide) was applied to the same powder to eliminate the epoxy resin. Following this, copper was totally removed by agitating the sample with 1 M acetic acid and 5 mL of H_2O_2 (30% w/w in H_2O) solution for 2 hours. The glass fiber was carefully cleaned and collected after the copper was extracted as copper acetate. The extracted glass fiber (GF) was then ultrasonicated (250 W) for 45 minutes to reduce its size before being recovered by filtering. Finally, the GF was dried in a hot air oven at 105 °C and employed as a catalyst preparation support.

3.2.2. GaMo–GF catalyst preparation. Three gallium–molybdenum catalysts, namely Ga^2Mo–GF (containing 2 wt% Ga), Ga^4Mo–GF (containing 4 wt% Ga), and Ga^6Mo–GF (containing 6 wt% Ga), were synthesized by varying the gallium precursor loading with a fixed amount of molybdenum according to Table 5. The catalyst was made utilizing the wet impregnation process. 0.36 g of gallium(III) nitrate hydrate, 0.34 g of bis(acetylacetonate) dioxo-molybdenum(VI), and 5 g of GF were placed in 70 mL of acetone and agitated for 10 minutes under moderate heating to make a 4 wt% catalyst. After 10 minutes, 2 mL of ammonium hydroxide was added, and the mixture was agitated for another 40 minutes under gentle heating. The mixture was kept overnight before being ultra-sonicated for 30 minutes to facilitate nano-impregnation. The mixture was then filtered, and the residue was oven dried at 80 °C for 24 hours. The oven-dried powder was then calcined for 2 hours at 700 °C (calcination temperature was determined through TGA analysis).

3.3. Catalyst efficacy assessment in hydrolysis of delignified corncob (DCC)

Hydrolysis of DCC (details of delignification of corncob are given in the Section, S1 (ESI†)) was performed in a quartz–halogen solar batch reactor (QHSR, 200 W) employing the prepared catalysts to investigate the efficacy of the prepared photocatalysts. In an experimental run, 250 mg of delignified corn cob (DCC) was measured and added to 20 mL of distilled water in a single necked round bottom flask (50 mL) equipped with a centrally fitted stirrer. Subsequently, a specified quantity of prepared photocatalysts was added to the aforementioned mixture (Table 5). The reaction mixture was stored under dark conditions at 25 °C for 20 minutes before the photocatalytic reaction to achieve adsorption equilibrium. Thereafter, radiation was applied and the mixture was rotated at 500 rpm. A PID controller was used to keep the temperature stable.

3.3.1. Design and optimization of the DCC hydrolysis process. The DCC hydrolysis process was designed according to Taguchi orthogonal design (L9 TgOD) (using Minitab Inc. software), where four independent process control parameters, namely reaction temperature (R_T), time (R_t), catalyst concentration (C_c), and gallium (Ga) precursor loading (P_L), were used to monitor the photocatalytic hydrolysis process (Table 5). Notably, the levels of the four process factors were selected based on the preliminary results from individual factorial experiments. According to L9 TgOD, a total of nine experimental runs (Table 6) were conducted with different parametric combinations and the impacts of the four process parameters on the DCC degradation process were analyzed and adjusted. The best process variables corresponding to the maximal FS yield (Y_{FS}) were identified using the "bigger is better" criteria to evaluate signal-to-noise (SN) ratios (eqn (2)) and analysis of variance (ANOVA).

$$\text{SN ratio} = -10\log\left(\frac{1}{n}\sum_{m-1}^{n}\frac{1}{Y_{FS,m}{}^2}\right) \quad (2)$$

where n represents the number of experiments done using a specific set of parameters (Table 6), m reflects the number of repetitions, and $Y_{FS,m}$ is the Y_{FS} related to run m.

3.4. Estimation of fermentable sugar

A Waters HPLC system with an RI detector (PerkinElmer 200 series) and a Waters carbohydrate column were used for the chromatographic separation of fermentable sugars. The furfural and acidic by product concentrations in the hydrolysate were analyzed using a UV detector and C18 column. A mobile phase of acetonitrile and water (60 : 40, v/v) with a flow rate of

Table 5 Independent process parameters and levels for photocatalytic hydrolysis of DCC

Factors	Units	L_{-1} Level	L_0 Level	L_1 Level
Reaction temp. (R_T)	°C	80	90	100
Ga precursor loading (P_L)	wt%	2	4	6
Catalyst concentration (C_c)	wt%	5	10	15
Reaction time (R_t)	min	20	30	40

Table 6 L9 TgOD for photocatalytic hydrolysis of DCC using GaMo–GF catalysts

Experimental runs	R_T (°C)	R_t (min)	C_c (wt%)	P_L (wt%)	FS yield (mol%)
1	80	20	5	2	25.12
2	80	30	10	4	45.16
3	80	40	15	6	51.93
4	90	20	10	6	56.24
5	90	30	15	2	63.39
6	90	40	5	4	53.91
7	100	20	15	4	72.47
8	100	30	5	6	53.31
9	100	40	10	2	52.43

1 mL min^{-1} was used for both the detectors. The calibration plots of the corresponding standard constituents were used to calculate the concentrations of the hydrolysate constituents. At the completion of each analysis, the column was rinsed with the said mobile phase for more than 30 minutes. Finally, eqn (3) has been used to determine the yield of FS (Y_{FS})

$$Y_{FS}(\text{mol}\%) = \left[\frac{(m_g + (m_{cl} \times 1.053))}{m_c \times 1.111} + \frac{(m_x + m_a)}{m_h \times 1.136}\right] \times 100 \quad (3)$$

where m_g = mass of glucose (g), m_{cl} = mass of cellobiose (g), m_x = mass of xylose (g), m_a = mass of arabinose (g), m_c = mass of cellulose (g), m_h = mass of hemicellulose (g). The mass buildup during the hydrolysis of cellulose to glucose, cellobiose to glucose and hemicellulose to xylose and arabinose, respectively, is represented by the multiplication factors 1.111, 1.053, and 1.136.[60] The compositions of corncob and DCC are provided in the Section, S2 (ESI†).

3.5. Characterization of the synthesized catalyst

The properties of the prepared GaMo–GF photocatalysts and GF support were investigated employing various characterization techniques. First, TGA analysis was performed using a PerkinElmer, Pyris Diamond TG/DTA analyzer with N_2 flow (1.2 L h^{-1}) at a heating rate of 10.0 °C min^{-1} from 25 °C to 800 °C. The photocatalytic characteristics of the optimum GaMo–GF catalyst were investigated using a PerkinElmer LAMBDA 950 UV-vis-NIR spectrophotometer with a tungsten halogen lamp as the light source. X-ray diffraction (XRD) patterns of the GF support and the prepared catalysts were obtained on a Bruker D8 Advance diffractometer employing Cu Kα radiation with a wavelength of 1.5147 Å. The GaMo–GF's infrared spectra were also recorded using an FTIR-Shimadzu (Alpha) instrument in a wavelength range of 400 to 4000 cm^{-1}. To determine the surface area as well as pore volume of the prepared catalysts, BET analysis was done using a NOVA touch 2LX. FESEM (JSM-6360 (JEOL Ltd.) at 15 kV and HRTEM were also used to investigate the surface morphology of the optimum GaMo–GF catalyst. Elemental analysis and mapping were performed on a Bruker XFlash® 6 detector series using EDAX analysis. X-ray photoelectron spectroscopy (XPS) of the optimum GaMo–GF was used to measure the binding energy as well as oxidation state of various elements contained in the catalyst specimen. The samples' acidity was determined by NH_3-TPD analysis (Quanta Chrome Instruments, TPR win v2).

3.6. Detoxification of the hydrolysate

After concentrating the hydrolysate through vacuum evaporation, the detoxification of the DCC hydrolysate was done employing various detoxification methods. Neutralization with NaOH (pH: 6.5–7.00), over-liming with Ca $(OH)_2$ (pH: 10), solvent extraction, and the ion exchange method were employed to detoxify the optimally produced DCC hydrolysate. For solvent extraction, ethyl acetate was used as extracting solvent and for ion exchange and the Amberlite IRP69 resin (Ca^{2+}) was used to extract the impurities present in the hydrolysates. Moreover, the ion exchange resin treatment was done in a chromatographic column (bed length: 25 cm; diameter: 10 mm) packed with the Amberlite IRP69 resin (Ca^{2+}) of 25 g and a peristaltic pump was used to control the hydrolysate flow rate in the chromatographic column (~0.5 mL min^{-1}). The effluent was collected at constant intervals and analysed using HPLC.

3.7. Inoculation of *Pichia stipitis* and fermentation of the detoxified hydrolysate

First, the collected *Pichia stipitis* NCIM 3499 strain was cultured on an agar plate with a synthetic growth medium containing

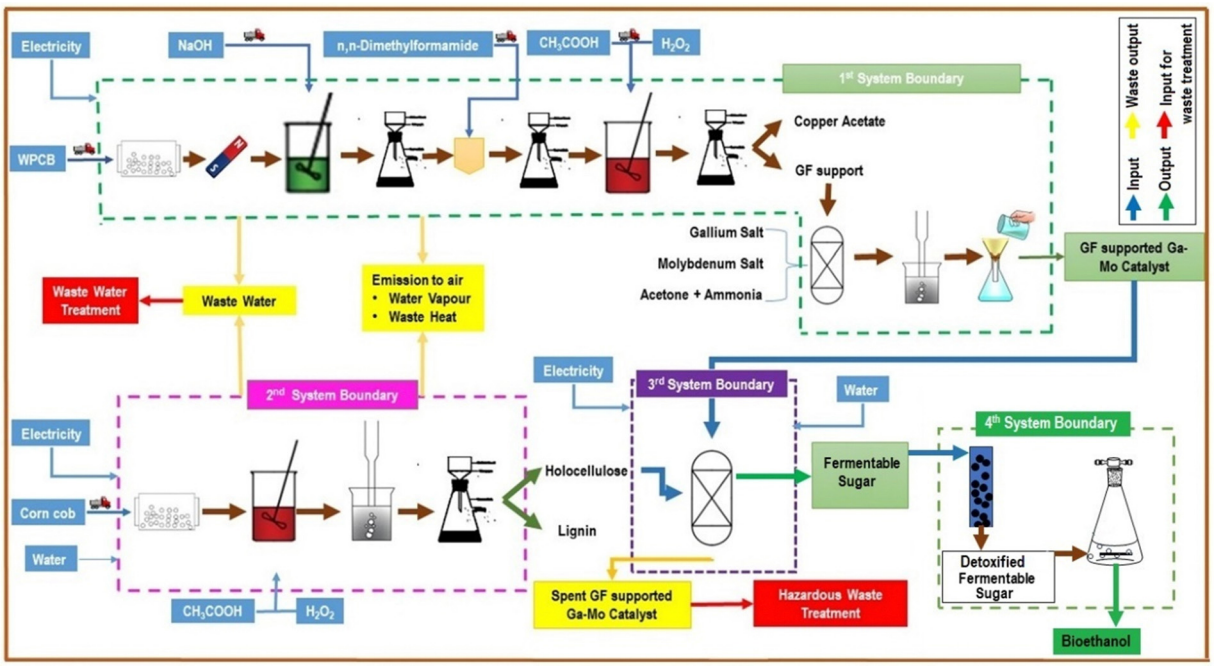

Fig. 15 System boundaries and the process flow diagram of LCA.

10 g L^{-1} yeast extract, 20 g L^{-1} peptone, 20 g L^{-1} xylose, and 20 g L^{-1} agar for 3 days at pH 5.0 ± 0.1 and temperature 30 °C. Afterwards, colonies from the plate were sub-cultured (Fig. 1S, ESI†) in a inoculum medium containing 10 g L^{-1} yeast extract, 0.5 g L^{-1} $(NH_4)_2SO_4$, 1.065 g L^{-1} $MgCl_2{\cdot}6H_2O$, 0.5 g L^{-1} KH_2PO_4 and 24 g L^{-1} xylose.[61] Afterward, the cells were collected and resuspended in water and the resulting cell suspension was then utilized as the inoculum for the fermentation process.

Finally, the fermentation process of detoxified DCC was carried out in an Erlenmeyer flask at 30 °C under shaking conditions (100 rpm). The fermentation medium is composed of 50 mL of detoxified DCC hydrolysates, 2 mL of inoculum, and 1 mL of nutrient solution as suggested by Agbogbo *et al.*, 2006.[62] During fermentation, samples were withdrawn at regular intervals of 4 h and centrifuged for 15 min at 4 °C. The cell free supernatant was used to determine the bioethanol and residual sugar concentrations.

3.8. Life-cycle assessment

The environmental impacts associated with each process steps were evaluated using OpenLCA 1.11.0 software. The whole process flow and system boundaries for LCA are depicted in a schematic in Fig. 15. The system has been divided into four boundaries. The 1st system boundary includes the extraction of GF from W-PCBs and the preparation of the GaMo–GF photocatalyst. The 2nd system boundary comprises the processing and delignification of the corncob, in which, life cycle inventory results are evaluated based on the manufacturing of 1 kg of DCC. The 3rd system boundary incorporates the photocatalytic hydrolysis process where the life cycle inventory results are evaluated based on the manufacturing of 1 kg of FS. Finally, the 4th system boundary incorporates the detoxification and fermentation step, where the life cycle inventory results are evaluated based on the manufacturing of 1 kg of bioethanol. The study findings have been up-scaled as per the functional units and provided as a database for the said life cycle inventory (LCI). LCI data derived from the process were tabulated in the supplementary document (Tables S4–S10, ESI†).

After preparing the LCI database, the ReCiPe Midpoint (H) [v1.11] method was employed to assess the potential environmental impacts associated with each process. Furthermore, a comparative LCA analysis was also conducted to determine the most environment friendly DCC hydrolysate detoxification approach for the production of bioethanol.

4. Conclusion

A W-PCB derived cost-effective glass fiber (GF) supported gallium–molybdenum (GaMo–GF) photo-catalyst demonstrated remarkable efficacy in the conversion of fermentable sugars, leading to successful bioethanol production through fermentation with *Pichia stipitis*. Experimental findings demonstrated that the synthesized Ga^4Mo–GF catalyst effectively hydrolyzed the delignified corncob (DCC) in a tungsten-halogen irradiated batch reactor, yielding a 78.35 mol% FS under mild optimized conditions: 100 °C and 30 min. The comparative hydrolysate detoxification study revealed that the maximum removal of inhibitors, such as furfural (86%), formic acid (92%), and levulinic acid (95%), could be achieved using the Amberlite IRP69 cation resin compared to other detoxification methods while contributing to less environmental impacts on environmental imapct indicators, such as climate change, fossil depletion, metal depletion, and water depletion. Additionally, the Amberlite IRP69 cation resin detoxified hydrolysate provided a higher bioethanol concentration (4.32 mmol mL^{-1}) compared to the other detoxification methods such as NaOH neutralization (3.06 mmol mL^{-1}), Ca $(OH)_2$ over-liming (2.88 mmol m^{-1}), and ethyl acetate solvent extraction (3.73 mmol mL^{-1}) when fermented with *Pichia stipitis*. Moreover, the optimized Ga^4Mo–GF catalyst exhibited reusability for up to 7 cycles in the DCC hydrolysis process, showcasing both its stability and the consequential reduction in environmental impacts throughout the corncob to bioethanol conversion process.

Author contributions

Aritro Sarkar: data curation, formal analysis, investigation, methodology, writing – original draft; Sourav Barman: conceptualization, data curation, formal analysis, investigation. methodology, software, visualization, writing – original draft; and Rajat Chakraborty: conceptualization, funding acquisition, project administration, supervision, validation, writing – reviewing and editing.

Data availability

Supporting data for the findings are available in the ESI† of this manuscript (YA-ART-04-2024-000226).

Conflicts of interest

The authors have no conflicts of interest.

Acknowledgements

The financial support of DHESTBT (ST/P/S&T/4G-2/2018) (Government of West Bengal, India) is gratefully acknowledged.

References

1 V. Forti, C. P. Baldé, R. Kuehr and G. Bel, United Nations University (UNU), International Telecommunication Union (ITU) & International Solid Waste Association (ISWA), Bonn/Geneva/Rotterdam, 2020, 120.
2 Y. Shen, R. Zhao, J. Wang, X. Chen, X. Ge and M. Chen, *Waste Manage.*, 2016, **49**, 287–303.
3 A. Cesaro, A. Marra, V. Belgiorno and M. Guida, *J. Cleaner Prod.*, 2017, **142**, 2656–2662.
4 M. Oguchi, H. Sakanakura and A. Terazono, *Sci. Total Environ*, 2013, **463**, 1124–1132.

5 C. Quan, A. Li and N. Gao, *J. Anal. Appl. Pyrolysis*, 2010, **89**, 102–106.
6 P. Zhou, J. Barford and G. McKay, *Financial & Business Management (IFBM)*, 2013, **1**, 126–135.
7 Y. Kan, Q. Yue, J. Kong, B. Gao and Q. Li, *Chem. Eng. J.*, 2015, **260**, 541–549.
8 S. Barman and R. Chakraborty, *ACS Omega*, 2018, **3**, 18499–18509.
9 C. Guan, Y. Tao, S. Chen, J. Zhu and X. Gao, *Environ. Sci. Pollut. Res.*, 2021, **28**, 46281–46290.
10 O. Erenstein, M. Jaleta, K. Sonder, K. Mottaleb and B. M. Prasanna, *Food Secur.*, 2022, **14**, 1295–1319.
11 Q. Qing, Q. Guo, P. Wang, H. Qian, X. Gao and Y. Zhang, *Bioresour. Technol.*, 2018, **260**, 150–156.
12 X. Gong, Q. Li, T. Li, C. Li, J. Huang, N. Zhou and X. Jia, *Ind. Crops Prod.*, 2022, **176**, 114317.
13 A. Nagarajan, B. Thulasinathan, P. Arivalagan, A. Alagarsamy, J. B. Muthuramalingam, S. D. Thangarasu and K. Thangavel, *Bioresour. Technol.*, 2021, **340**, 125677.
14 B. Qi, A. Vu, S. R. Wickramasinghe and X. Qian, *Biomass Bioenergy*, 2018, **117**, 137–145.
15 N. Chen, G. Zhang, P. Zhang, X. Tao, Y. Wu, S. Wang and M. Nabi, *Bioresour. Technol.*, 2019, **292**, 121915.
16 L. Wan, Z. Gao, B. Wu, F. Cao, M. Jiang, P. Wei and H. Jia, *Appl. Biochem. Biotechnol.*, 2021, **193**, 205–217.
17 S. Banerjee, S. Mudliar, R. Sen, B. Giri, D. Satpute, T. Chakrabarti and R. A. Pandey, *Biofuels, Bioprod. Biorefin.*, 2010, **4**, 77–93.
18 J. C. Du Preez, M. Bosch and B. A. Prior, *Appl. Microbiol. Biotechnol.*, 1986, **23**, 228–233.
19 M. L. M. Villarreal, A. M. R. Prata, M. G. A. Felipe and J. A. E. Silva, *Enzyme Microb. Technol.*, 2006, **40**, 17–24.
20 A. K. Chandel, R. K. Kapoor, A. Singh and R. C. Kuhad, *Bioresour. Technol.*, 2007, **98**, 1947–1950.
21 M. Kashid and A. Ghosalkar, *3 Biotech*, 2017, **7**, 1–9.
22 P. Selvakumar, A. A. Adane, T. Zelalem, B. M. Hunegnaw, V. Karthik, S. Kavitha, M. Jayakumar, N. Karmegam, M. Govarthanan and W. Kim, *Fuel*, 2022, **321**, 124060.
23 H. G. Yücel and Z. Aksu, *Fuel*, 2015, **158**, 793–799.
24 F. Liu, X. Guo, Y. Wang and G. Chen, *J. Cleaner Prod.*, 2021, **329**, 129707.
25 G. Murali and Y. Shastri, *Biofuels*, 2022, **13**, 237–247.
26 S. Banerjee, C. Pandit, M. P. Gundupalli, S. Pandit, N. Rai, D. Lahiri, K. K. Chaubey and S. J. Joshi, *Environment, Development and Sustainability*, 2023, pp. 1–32.
27 D. Sundeep, A. Gopala Krishna, R. V. Ravikumar, T. Vijaya Kumar, S. Daniel Ephraim and Y. L. Pavan, *Int. Nano Lett.*, 2016, **6**, 119–128.
28 N. Iqbal, I. Khan, Z. H. Yamani and A. Qurashi, *Sci. Rep.*, 2016, **6**, 32319.
29 J. Zhang, C. Xia, Q. Deng, W. Xu, H. Shi, F. Wu and J. Xu, *J. Phys. Chem. Solids*, 2006, **67**, 1656–1659.
30 I. M. Joni, L. Nulhakim, M. Vanitha and C. Panatarani, *Journal of Physics: Conference Series*, IOP Publishing, 2018, vol. 1080, p. 012006.
31 O. Roy, S. Roy Choudhury and R. Chakraborty, *Environ. Sci. Pollut. Res.*, 2023, **30**, 25506–25522.
32 Y. Liang, J. Ouyang, H. Wang, W. Wang, P. Chui and K. Sun, *Appl. Surf. Sci.*, 2012, **258**, 3689–3694.
33 Z. Han, F. Zhou, Y. Liu, K. Qiao, H. Ma, L. Yu and G. Wu, *J. Taiwan Inst. Chem. Eng.*, 2019, **103**, 149–159.
34 C. Schramm, *Spectrochim. Acta, Part A*, 2020, **243**, 118815.
35 M. A. Poiana, E. Alexa, M. F. Munteanu, R. Gligor, D. Moigradean and C. Mateescu, *Open Chem.*, 2015, **13**, 689–698.
36 P. Y. Bruice, *Org. Chem.*, 2011, **2620**, A16–A17.
37 Y. Cheng, J. Chen, K. Yang, Y. Wang, Y. Yin, H. Liang and G. Du, *J. Vac. Sci. Technol., B: Nanotechnol. Microelectron.: Mater., Process., Meas., Phenom.*, 2014, **32**, 3.
38 A. Khojastehnezhad, F. Moeinpou and M. Vafaei, *J. Mex. Chem. Soc.*, 2015, **59**, 29–35.
39 F. Barontini, K. Marsanich, L. Petarca and V. Cozzani, *Ind. Eng. Chem. Res.*, 2005, **44**, 4186–4199.
40 V. Berbenni, C. Milanese, G. Bruni and A. Marini, *J. Therm. Anal. Calorim.*, 2005, **82**, 401–407.
41 K. Zhou, S. Jiang, C. Bao, L. Song, B. Wang, G. Tang, Y. Hu and Z. Gui, *RSC Adv.*, 2012, **2**, 11695–11703.
42 C. C. Hu and H. Teng, *J. Phys. Chem. C*, 2010, **114**, 20100–20106.
43 L. S. Yoong, F. K. Chong and B. K. Dutta, *Energy*, 2009, **34**, 1652–1661.
44 J. Zhao, A. Jayakumar and J. M. Lee, *ACS Sustainable Chem. Eng.*, 2018, **6**, 2976–2982.
45 B. Demri and D. Muster, *J. Mater. Process. Technol.*, 1995, **55**, 311–314.
46 M. Tang, A. T. Nelson, E. S. Wood, S. A. Maloy and Y. B. Jiang, *Scr. Mater.*, 2016, **120**, 49–53.
47 J. Shah, P. Ratnasamy and M. L. Carreon, *Catalysts*, 2017, **7**, 372.
48 Y. Wu, Z. Fu, D. Yin, Q. Xu, F. Liu, C. Lu and L. Mao, *Green Chem.*, 2010, **12**, 696–700.
49 Y. Jiang, X. Li, X. Wang, L. Meng, H. Wang, G. Peng, X. Wang and X. Mu, *Green Chem.*, 2012, **14**, 2162–2167.
50 L. Wang, Z. Zhang, L. Zhang, S. Xue, W. O. Doherty, I. M. O'Hara and X. Ke, *RSC Adv.*, 2015, **5**, 85242.
51 Z. Zhang and Z. Zhao, *Carbohydr. Res.*, 2009, **344**, 2069–2072.
52 L. Shuai and X. Pan, *Energy Environ. Sci.*, 2012, **5**, 6889–6894.
53 H. Cai, C. Li, A. Wang, G. Xu and T. Zhang, *Appl. Catal., B*, 2012, **123**, 333–338.
54 J. P. Delgenès, R. Moletta and J. M. Navarro, *Appl. Microbiol. Biotechnol.*, 1991, **35**, 656–661.
55 C. C. Okonkwo, M. M. Azam, T. C. Ezeji and N. Qureshi, *Bioprocess Biosyst. Eng.*, 2016, **39**, 1023–1032.
56 A. K. Chandel, J. Q. Albarelli, D. T. Santos, S. P. Chundawat, M. Puri and M. A. Meireles, *Biofuels, Bioprod. Biorefin.*, 2019, **13**, 994–1014.
57 P. V. Vikash, P. V. Mandade and Y. Shastri, *Environ. Prog. Sustainable Energy*, 2018, **37**, 2165–2174.
58 S. Macrelli, J. Mogensen and G. Zacchi, *Biotechnol. Biofuels*, 2012, **5**, 1–8.
59 T. Moyo, B. H. Chirume and J. Petersen, *Resour., Conserv. Recycl.*, 2020, **152**, 104545.
60 S. Barman and R. Chakraborty, *AIChE J.*, 2019, **65**, e16677.
61 J. N. Nigam, *J. Biotechnol.*, 2001, **87**, 17–27.
62 F. K. Agbogbo, G. Coward-Kelly, M. Torry-Smith and K. S. Wenger, *Process Biochem.*, 2006, **41**, 2333–2336.